

PAPER

Structural transformations and physical properties of $(1 - x)$ $\text{Na}_{0.5}\text{Bi}_{0.5}\text{TiO}_3 - x \text{BaTiO}_3$ solid solutions near a morphotropic phase boundary

To cite this article: Hari Sankar Mohanty *et al* 2019 *J. Phys.: Condens. Matter* **31** 075401

View the [article online](#) for updates and enhancements.



IOP | ebooks™

Bringing you innovative digital publishing with leading voices
to create your essential collection of books in STEM research.

Start exploring the collection - download the first chapter of
every title for free.

Structural transformations and physical properties of $(1 - x) \text{Na}_{0.5}\text{Bi}_{0.5}\text{TiO}_3 - x \text{BaTiO}_3$ solid solutions near a morphotropic phase boundary

Hari Sankar Mohanty¹, Tapabrata Dam¹, Hitesh Borkar²,
Dhiren K Pradhan³, K K Mishra⁴, Ashok Kumar², Balaram Sahoo⁵ ,
Pawan K Kulriya⁶, C Cazorla⁷, J F Scott⁸  and Dillip K Pradhan^{1,9} 

¹ Department of Physics and Astronomy, NIT Rourkela, Rourkela, Odisha 769008, India

² CSIR-National Physical Laboratory, Dr K S Krishnan Marg, New Delhi 110012, India

³ Geophysical Laboratory, Carnegie Institution for Science, Washington, DC 20015, United States of America

⁴ Department of Physics and Institute for Functional Nanomaterials, University of Puerto Rico, San Juan, PR 00936, United States of America

⁵ Materials Research Centre, Indian Institute of Science, Bangalore 560012, India

⁶ Materials Science Group, Inter-University Accelerator Centre, New Delhi 110 067, India

⁷ School of Materials and Engineering, UNSW Sydney, Sydney, NSW 2052, Australia

⁸ Department of Chemistry and Department of Physics, University of St. Andrews, St. Andrews KY16 9ST, United Kingdom

E-mail: dillip.pradhan79@gmail.com

Received 29 October 2018, revised 16 November 2018

Accepted for publication 26 November 2018

Published 31 December 2018



CrossMark

Abstract

Piezoelectric and other physical properties are significantly enhanced at (or near) a morphotropic phase boundary (MPB) in ferroelectrics. MPB materials have attracted significant attention owing to both fundamental physics as well as the possibility of well-regulated energy and information storage devices which are dominated by lead (Pb)-based materials. Here, we report the crystal structure, Raman spectra, dielectric constant and polarization near the MPB of lead free $(1 - x) \text{Na}_{0.5}\text{Bi}_{0.5}\text{TiO}_3 - x \text{BaTiO}_3$ ($0.00 \leq x \leq 0.10$) solid-solution, prepared by sol-gel auto combustion technique and sintered by microwave sintering technique. With the addition of BaTiO_3 into $\text{Na}_{0.5}\text{Bi}_{0.5}\text{TiO}_3$, it induces a structural phase transition from $R3c$ (a single phase) to $R3c + P4mm$ (a dual phase) close to $x = 0.06$ and 0.07 and transform to a high symmetry tetragonal phase $P4mm$ at higher compositions ($x = 0.08$ to 0.10) as evident from our x-ray Rietveld refinement and Raman spectroscopic results. We perform first-principles calculations based on density functional theory that confirm a structural transition from a rhombohedral to a tetragonal phase under increasing x . In the prepared solid solution, an anomalous enhancement of remnant polarization ($2P_r^0$) was observed for $x = 0.06$ and 0.07 , which has been explained based on the existence of the MPB. On the other hand, the value of coercive field E_C^0 was found to be decreased linearly from $x = 0.00$ to 0.06 ; it is constant for higher compositions. Further details of the ferroelectric properties on the electric field poled samples have been studied and compared with the as-grown (unpoled) samples.

⁹ Author to whom any correspondence should be addressed.

Keywords: lead-free ferroelectric materials, NBT–BT solid solution, morphotropic phase boundary, first-principles calculations, microwave sintering, crystal structure

 Supplementary material for this article is available [online](#)

(Some figures may appear in colour only in the online journal)

1. Introduction

Since the discovery of ferroelectric behaviour in BaTiO_3 , ferroelectric ceramic oxides of various structural families have been widely used in various devices such as actuators, transducers, micro-electromechanical systems, filters, resonator, multilayer capacitors, and memory devices such as non-volatile ferroelectric random access memory [1–3]. Among different structural families of ferroelectric oxides, perovskites are mostly used because of their simple structure and the possibility of tuning the physical properties for the requirement of device applications [2]. For a long time, the market-dominating lead-based perovskite ferroelectric ceramics have been used widely for device applications. However, due to the toxic nature of lead, an effort has been made to develop lead-free ferroelectric materials [4]. The lead-free ferroelectric systems belonging to the perovskite structure, such as BaTiO_3 (BT), $(\text{Na}_{1/2}\text{Bi}_{1/2})\text{TiO}_3$ (NBT), $(\text{Bi}_{1/2}\text{K}_{1/2})\text{TiO}_3$ (BKT), NaNbO_3 , SrTiO_3 , KNbO_3 have been studied widely [1, 4, 5]. Although investigation on several lead free-perovskite systems has been reported, the $(\text{Na}_{1/2}\text{Bi}_{1/2})\text{TiO}_3$ (NBT) system attracted special attention in recent years due to its relatively good ferroelectric and dielectric properties. NBT is strongly ferroelectric with Curie temperature $T_C \sim 320^\circ\text{C}$ (with a diffuse phase transition), and possesses remnant polarization $P_r \sim 38 \mu\text{C cm}^{-2}$ and coercive field $E_c \sim 73 \text{ kV cm}^{-1}$ at room temperature [5, 6]. However, the major drawbacks are high conductivity and dielectric loss along with high coercive field (i.e. 73 kV cm^{-1}), which cause problems during poling [7]. To overcome these problems, various methodologies have been adopted by different research groups, such as (i) fabrication of solid solutions with other perovskite compounds [5, 8], (ii) substitutions at *A*/ or and *B*-sites, and (iii) various synthesis processes to produce high-quality materials. Although the preparation of solid solutions and substitution are effective to some extent to improve the material performance, we still need to improve its properties to meet the requirements for practical uses. Therefore, it is imperative to develop high-quality NBT-based ceramics.

NBT and NBT-based materials are usually prepared using a conventional solid-state reaction and conventional sintering technique at high temperature ($\geq 1100^\circ\text{C}$) and longer sintering time to obtain a single phase material with dense microstructure. Often such a preparation method involving higher temperature results in a nonstoichiometric product due to the volatile nature of Na and Bi cations. Due to a longer sintering time, the microstructure of the materials gives rise to abnormal grain growth with non-uniform distribution of grain sizes [9, 10]. These factors result in high dielectric loss and high conductivity. To obtain the ferroelectric materials

with improved properties, synthesis of high-quality ceramic powders with exact stoichiometry is the essential requirement. It is established that microwave sintering has many advantages over conventional sintering: rapid and uniform heating rate, cost-effectiveness, lower sintering temperature, a considerable reduction in sintering time, enhanced densification rate and improved microstructure [11]. Microwave sintering is expected to give an excellent and uniform grains distribution. Certainly, Ramana *et al* prepared the lead-free NBT ceramics using both microwave and conventional sintering methods and observed that microwave sintering offers a potential advantage over the latter, with higher dielectric constant, uniform grain size, lower sintering temperature and time, and higher piezoelectric (d_{33}) coefficient [10]. Meanwhile, for various device applications ferroelectric ceramics oxides require electrical poling [2, 12, 13]. There are several publications available on the effect of electrical poling on microstructure and functional properties of many perovskite ceramics regarding domain dynamics, domain switching, charge migration and grain boundary reduction [13, 14]. Different types of electrical poling methods are usually employed to polarize the ferroelectric ceramics: poling below the coercive field, electromechanical poling, high-temperature poling, and short- and long-time duration poling [15–17]. Out of these, the most accepted poling procedure to obtain stable polarization and enhanced piezoelectric properties is by poling the sample near T_C , below the coercive field, for a shorter time [12, 18]. To achieve optimal piezoelectricity, electrical poling has been carried out on solid solutions of BaTiO_3 , $\text{Pb}(\text{Zr}_x\text{Ti}_{1-x})\text{O}_3$ and BNT-BT based compositions below the coercive field [17]. Picht *et al* studied the structural properties of unpoled and poled lead-free $(1-x)\text{Bi}_{0.5}\text{Na}_{0.5}\text{TiO}_3 - x\text{BaTiO}_3$ ($0 \leq x \leq 0.2$) ceramics using XRD analysis. They observed a significant variation in lattice parameters for poled and unpoled samples and suggested the existence of a morphotropic phase boundary (MPB) in the composition range $0.06 \leq x \leq 0.08$ [19]. Maurya *et al* studied the effect of poling on the *A*-site disordered lead-free piezoelectric at morphotropic phase boundary composition of 0.93NBT–0.07BT using high-resolution transmission electron microscopy, neutron pair distribution function, Raman and dielectric spectroscopic studies. They found that electrical poling has the synergic effect of a change in octahedral tilt and cation displacement disorders which lead to structural transformations [16]. Ma *et al*, studied the effect of electrical poling on NBT–BT piezoelectric materials around MPB using *in situ* transmission electron microscopy (TEM) technique. They observed that strong piezoelectricity is associated with ferroelectric materials around MPB, can be created,

destroyed, or even replaced by another MPB through phase transitions during electrical poling [13].

To the best of our knowledge, the effects of electrical poling on the ferroelectric and electrical properties of NBT–BT solid solutions around the MPB region have not been investigated systematically. The correlation of enhancement of ferroelectric properties around MPB with crystallographic structure neither is well understood. In this article, we experimentally investigate the effects of electrical poling on the ferroelectric behaviour, lattice phonon vibrations, and structural properties of microwave sintered NBT–BT solid solutions over the composition range $0.00 < x < 0.10$. Temperature-dependent dielectric properties have also been investigated to ascertain the existence of different phase transition temperatures and their correlation with the crystal structure at MPB. In addition, first-principles simulations are carried out to gather further microscopic insight into the structural features of the competitive phases.

2. Experimental details

Polycrystalline ceramic oxides of $(1 - x) \text{Na}_{0.5}\text{Bi}_{0.5}\text{TiO}_3 - x \text{BaTiO}_3$ (NBT–BT) with $x = 0.00, 0.02, 0.04, 0.05, 0.06, 0.07, 0.08,$ and 0.10 were synthesized by sol–gel auto combustion route and sintered using microwave sintering technique. High purity precursors such as NaNO_3 , $\text{Bi}(\text{NO}_3)_3 \cdot 5\text{H}_2\text{O}$, $\text{Ti}[\text{OCH}(\text{CH}_3)_2]_4$, $\text{Ba}(\text{NO}_3)_2$, citric acid ($\text{C}_6\text{H}_8\text{O}_7$), glycine ($\text{C}_2\text{H}_5\text{NO}_2$) and ethylene glycol ($\text{C}_2\text{H}_6\text{O}_2$) were used for the synthesis of NBT–BT materials. In order to compensate the bismuth loss during calcinations/sintering process, a 5% excess of $\text{Bi}(\text{NO}_3)_3 \cdot 5\text{H}_2\text{O}$ was added for all compositions. The detailed experimental procedure for the synthesis of NBT–BT is reported elsewhere [20]. All the samples were calcined at 850°C for 6 h with a heating rate of 5°C min^{-1} in air, whereas they were sintered using a microwave furnace at 1000°C for 40 min with a heating rate of $20^\circ\text{C min}^{-1}$ in air. XRD data were collected at a scan rate of 2°min^{-1} over the Bragg angle range of 2θ ($10^\circ \leq \theta \leq 90^\circ$) using a powder x-ray diffractometer (Bruker D2 diffractometer with $\text{Cu-K}\alpha_1$ radiation) at room temperature. Raman spectroscopic measurements were carried out using 514.5 nm line of an Ar-ion laser covering the range $60\text{--}1000\text{ cm}^{-1}$ using a micro-Raman spectrometer (Invia, Renishaw, UK). Resolution of the spectrometer for 1800 l mm^{-1} grating is 2 cm^{-1} . Both surfaces of the pellet were electroded with silver paint. Before carrying out the dielectric and ferroelectric properties, the silver paint coated pellets were dried at 200°C for 2 h to remove the moisture if any present. Ferroelectric (P – E) hysteresis curves of ceramic pellets were collected at a frequency of 10 Hz with different applied voltages using a Radiant Ferroelectric Tester. The samples were poled in a silicone oil bath with the application of a DC electric field of 40 kV cm^{-1} for 1 h at RT. The dielectric properties have been studied as a function of temperature (from 30°C to 500°C) at selected frequencies (100 Hz to 1 MHz) using a computer-controlled impedance analyzer (HIOKI IM 3570) coupled with a home-made sample holder with an applied oscillating voltage of 1 V.

3. Results and discussion

3.1. Structural properties

Room temperature XRD patterns of $(1 - x) \text{Na}_{0.5}\text{Bi}_{0.5}\text{TiO}_3 - x \text{BaTiO}_3$ ($0.00 \leq x \leq 0.10$) are shown over a wide range of Bragg angles in figure 1. The XRD patterns are characterized by the presence of sharp and well-defined diffraction peaks, suggesting the formation of the well-sintered compounds. A close observation of these patterns indicates the absence of any additional peaks related to secondary phases, suggesting that the prepared powder samples are single-phase compounds. Rietveld refinement technique using freely available Fullprof software was used to analyse the XRD patterns of the samples as shown in figure 1 [20, 21]. In figure 1, the experimental data are shown as + (plus) symbol, the simulated data are presented as a continuous line. The Bragg peaks are represented as vertical lines and the difference between experimental and simulated XRD patterns are shown as continuous lines at bottom of the figure 1. The non-centro-symmetric $R3c$ space group (rhombohedral crystal structure in hexagonal setting) was used for Rietveld refinement of parent NBT and the refined pattern is presented in figure 1(a). We have observed a close match between the experimental and simulated data with χ^2 value ~ 2.92 . The lattice parameters obtained after refinement are $a = 5.4810$ (2) Å and $c = 13.4948$ (7) Å with unit cell volume $V = 351.09 \text{ Å}^3$, which are close to the reported values [22]. Interestingly, a small, weak super-lattice reflection around $2\theta = 38.5^\circ$ was noticed in the diffraction pattern of pure NBT system, as shown in figure 1(b). This is related to the symmetry involved in the non-centrosymmetric point group of the ferroelectric perovskite system, i.e. the relative positioning (tilting) of BO_6 octahedral with respect to other adjacent unit cells gives rise to super-lattice reflections [23]. These reflections are indexed to a double pseudo-cubic cell because the octahedral positioning (tilting) occurs in such a way that it leads to doubling of the unit cell. Often due to the low atomic scattering factor obtained from oxygen (low Z) and relatively small value of tilting amplitude, it is difficult to observe these reflections; and if at all visible, the intensity is quite poor [23]. This observed superlattice reflection corresponds to Miller indices $\frac{1}{2}(311)$, which are indexed as a pseudo-cubic cell. The rhombohedral crystal structure is characterized by the presence of $\frac{1}{2}$ (odd odd odd) miller index superlattice reflections, due to the anti-phase rotation of TiO_6 octahedra [22]. These all-odd index superlattice reflections are seen in diffraction patterns only when an out-of-phase rotation/tilt (according to Glazer notation) of the oxygen octahedral occurs about the three-fold axis of the rhombohedral cell [24]. Upon an increase in the BT concentration, the intensity of $\frac{1}{2}(311)$ superlattice reflection peak decreases; and for $x \geq 0.07$, it is observed to disappear, as shown in figure 1(b). Therefore, the Rietveld refinement was carried out using $R3c$ space group with hexagonal setting up to $x = 0.05$. Interestingly, with an increase in BT concentration x , a change in the peak position and peak broadening are observed. It can be mentioned here that Ma *et al* [13] reported the crystal structure of NBT–BT for $x = 0.06$ as the coexistence of

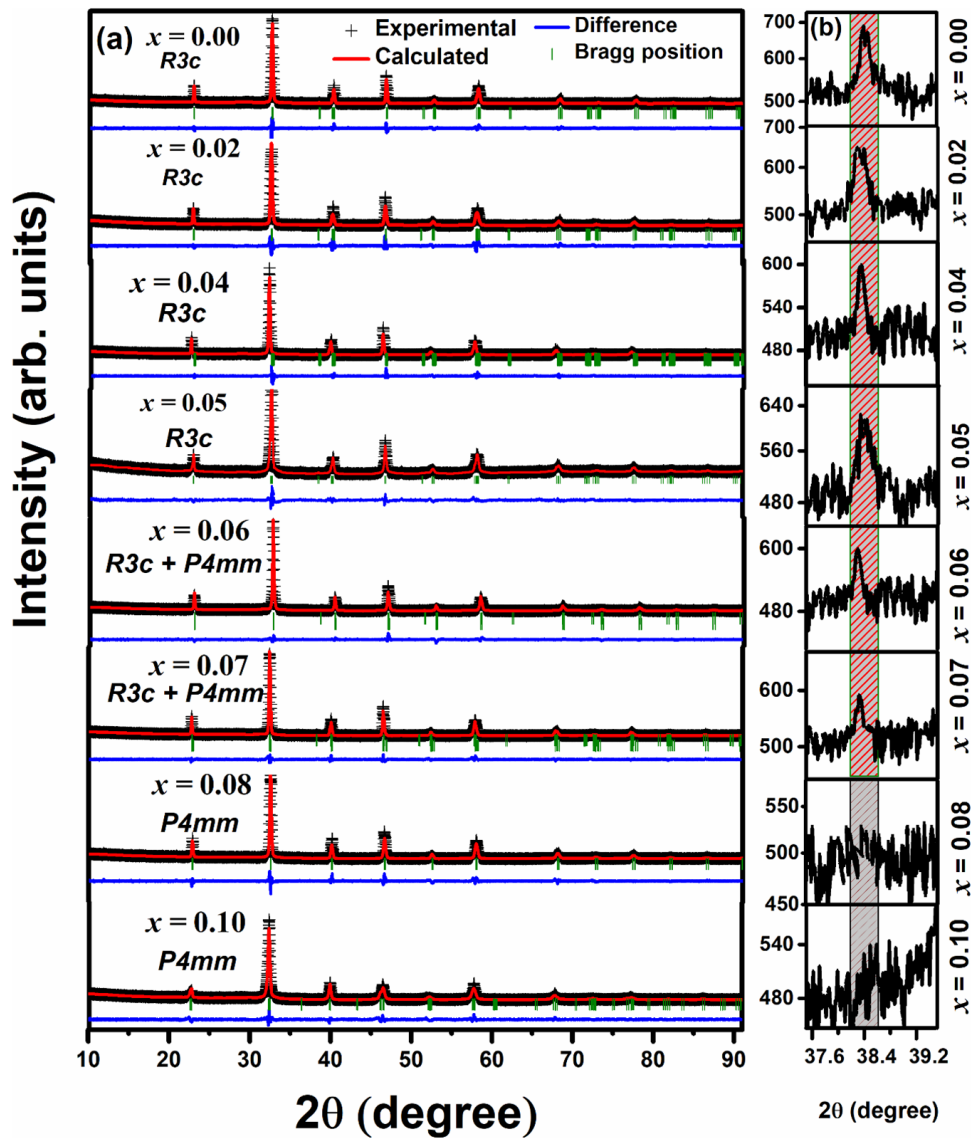


Figure 1. (a) and (b) Rietveld refined x-ray diffraction patterns of the solid solution $(1-x)$ NBT $-x$ BT for compositional range $(0.00 \leq x \leq 0.10)$ and amplified x-ray diffraction patterns in 2θ range $37.6^\circ \leq 2\theta \leq 39.2^\circ$ representing the super-lattice reflections respectively.

rhombohedral and tetragonal ($R3c + P4bm$) phases, whereas most recently using neutron diffraction experiment, Garg *et al* [25], reported the mixed phases of NBT–BT for $x = 0.065$ as $R3c + P4mm$. In view of this, we have fitted separately the data of NBT–BT for $x = 0.06$ and 0.07 using $R3c + P4bm$ and $R3c + P4mm$ and a better fit is observed in latter case, i.e. $R3c + P4mm$. With further increase in the BT concentrations, i.e. for $x = 0.08$ and 0.10 , we have fitted the XRD patterns with $P4mm$ space group. This is consistent with previous experimental and theoretical results reported by Ma *et al* [13], as well as with our first-principles calculations (presented in the next subsection). In the present case, compositional driven phase transitions from $R3c$ to $P4mm$ through the intermediate coexistence of $R3c + P4mm$ phases is observed. Rietveld refinement parameters are presented in supplementary material table S1 (stacks.iop.org/JPhysCM/31/075401/mmedia). The variation of phase fractions of $R3c$ and $P4mm$ phases with an increase in BT composition (x) obtained from our present

Rietveld refinement results is also shown in the supplementary material figure S1(a). With an increase in x up to 0.05 , the contribution of the rhombohedral phase is 100%. For $x = 0.06$ and 0.07 , a relatively less rhombohedral $R3c$ phase fraction such as 28%, and 16% are found, and a corresponding increase in the $P4mm$ phase fraction of 72%, 84% are estimated respectively. For $x = 0.08 - 0.10$, the tetragonal phase fraction is 100%. Since the present compositional driven phase transition from rhombohedral ($R3c$) to tetragonal ($P4mm$) phase does not obey the crystallographic group-subgroup relationship; hence the transition from rhombohedral-tetragonal must be first-order. Therefore, coexistence of crystallographic phases is expected in intermediate composition regions [26]. Sometimes coexistence of phases is observed around the MPB regions, but the interpretation of the details of the 1st order phase transition is not straightforward. Since $R3c$ and $P4mm$ crystallographic phases stabilize with similar free energy, the coexistence of these phases leading to flattening of the free

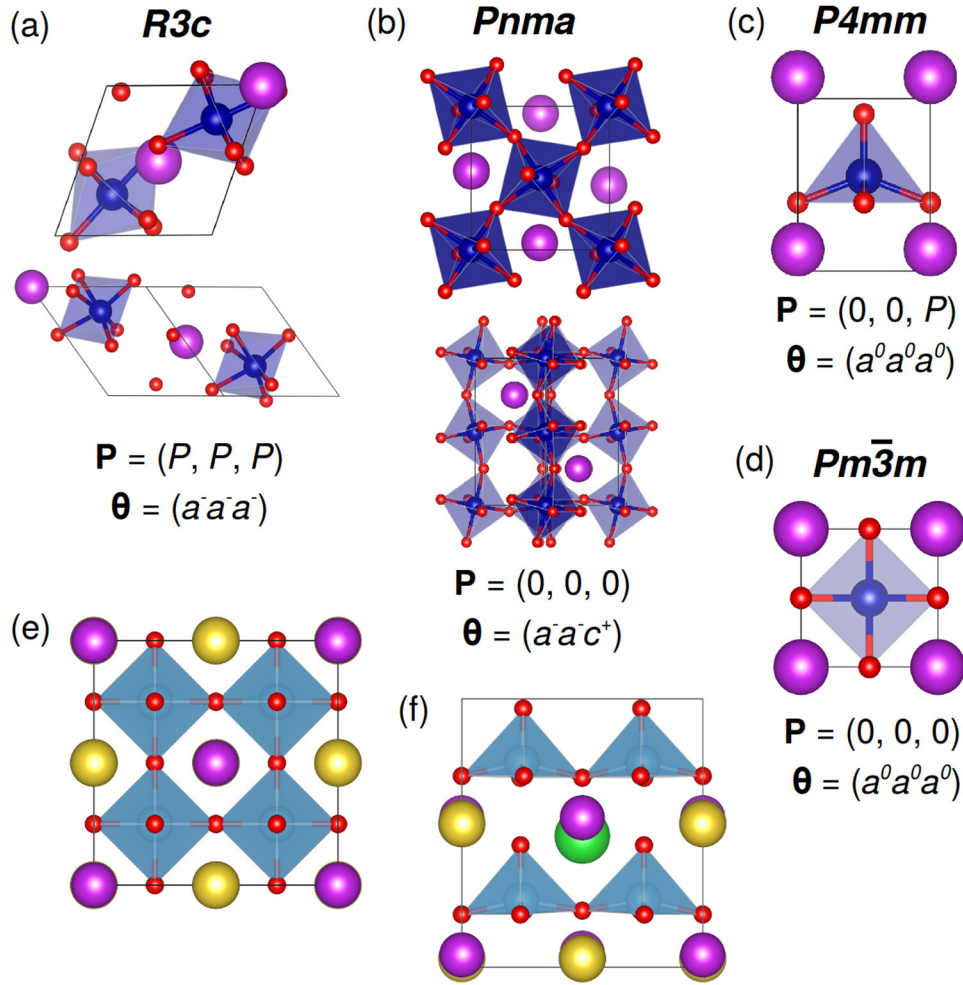


Figure 2. Structural models and corresponding features considered in our first-principles calculations. (a) Rhombohedral *R3c* phase. (b) Orthorhombic *Pnma* phase. (c) Tetragonal *P4mm* phase. (d) Cubic *Pm-3m* phase. *P* represents the electric polarisation in each structure expressed in pseudo-Cartesian components, and θ the pattern of the oxygen octahedral rotations expressed in Glazer's notation. (e) Simulation box and arrangement of Na and Bi ions over A-sites considered in our DFT calculations. (f) Zero-temperature equilibrium geometry determined for the (NBT)_{87.5}–(BT)_{12.5} system. Bi, Na, Ba, Ti, and O ions are represented with purple, yellow, green, blue, and red spheres, respectively.

energy curve justifies the possible existence of MPB around $x = 0.06$ and 0.07 in the present studies. Although *R3c* and *P4mm* crystallographic phases are present in these systems, they are pseudo-cubic regarding their lattice parameters (supplementary material table S1). The variation of unit cell volume for the rhombohedral and tetragonal phases has been plotted with the BT composition x , as shown in the supplementary material figure S1(b). One can see that the unit cell volume increases with x for both the rhombohedral and tetragonal phase. These increases in cell volume could be due to the substitution of larger ionic size Ba^{2+} cations (1.61 \AA) as compared to that of A-site [Na^{1+} (1.39 \AA) and Bi^{3+} (1.36 \AA)] cations [25].

3.1.1. Computational methods. We calculated the energetic and structural properties of bulk (NBT)_{1-x}–(BT)_x at $x = 0.0$ and 12.5% with first-principles methods based on density functional theory (DFT). We used the PBE variant of the generalized gradient approximation to DFT [27], as is implemented in the VASP package [28, 29]. The ‘projector augmented

wave’ method is employed to represent the ionic cores [30], and we considered the following electrons as valence: Na 3s, and 2p; Bi 5d, 6s, and 6p; Ti 3p, 4s, and 3d; Ba 5s, 5p, and 6s; and O 2s and 2p. Wave functions were represented in a plane-wave basis truncated at 650 eV , and we used a 40-atom simulation cell (equivalent to a $2 \times 2 \times 2$ replication of the typical five-atom perovskite unit cell) that allows us to reproduce the usual ferroelectric and anti-ferrodistortive distortions occurring in oxide compounds [31–34]. For integrations within the first Brillouin zone, we adopted a Gamma-centred k -point grid of $6 \times 6 \times 6$. Geometry relaxations were performed by using a conjugate-gradient algorithm that changed the volume and shape of the unit cell. The imposed tolerance on the atomic forces was 0.01 eV \AA^{-1} . By using these parameters, we obtain total energies that converged to within 0.5 meV per formula unit (f.u.).

3.1.2. Theoretical results. To further elucidate the atomic structure of bulk (NBT)_{1-x}–(BT)_x systems, we carried out first-principles calculations based on density functional

theory (DFT). In our theoretical analysis, we considered four different crystal structures that are commonly observed in ferroelectric oxide perovskites. Those structures are: (1) the rhombohedral $R3c$ phase characterised by an electric polarisation oriented along the pseudo-Cartesian direction $\langle 111 \rangle$ and oxygen octahedral rotations ($a^-a^-a^-$) in Glazer's notation (figure 2(a)), (2) the orthorhombic $Pnma$ phase with null electric polarisation and oxygen octahedral rotations ($a^-a^-c^+$) (figure 2(b)), (3) the tetragonal $P4mm$ structure characterised by an electric polarisation oriented along the pseudo-Cartesian direction $\langle 001 \rangle$ and null oxygen octahedral rotations (figure 2(c)), and (4) the cubic $Pm-3m$ structure with null electric polarisation and null oxygen octahedral rotations (figure 2(d)). Firstly, we sampled all possible ionic arrangements rendering a 50% Na/50% Bi A-site occupancy in a perfectly cubic 40-atom simulation cell. We found that the energetically most favourable configuration corresponds to placing each Na ion surrounded exclusively by Bi first-neighbours ions, and vice versa (figure 2(e)). In our subsequent calculations and for all structures, we constrained such a low-energy configuration over A sites.

In the $x = 0.0\%$ composition case, our DFT calculations predict that the rhombohedral $R3c$ phase is the ground state of the system, which is consistent with our observations. In particular, the energy of the $R3c$ phase is 22 meV/f.u. below that of the tetragonal $P4mm$ phase, 52 meV/f.u. below that of the orthorhombic $Pnma$ phase, and 446 meV/f.u. below that of the cubic $Pm-3m$ structure. Regarding the structural properties of the rhombohedral $R3c$ phase, we find the following equilibrium lattice parameters and volume: $a = b = 5.51 \text{ \AA}$, $c = 13.82 \text{ \AA}$, and $V = 363.1 \text{ \AA}^3$, which are in reasonably good agreement with our experimental data reported in table S1 of the supplementary information.

We simulated the $x = 12.5\%$ composition case by replacing one Na atom in the simulation cell (out of four) with one Ba ion since we found that Bi-ion substitutions were energetically less favourable in all the studied cases. Our DFT calculations predict that the tetragonal $P4mm$ phase is the ground state of the system (represented in figure 2(f)), which is also consistent with our experimental observations. In particular, the energy of the $P4mm$ phase is 54 meV/f.u. below that of the rhombohedral $R3c$ phase, 89 meV/f.u. below that of the orthorhombic $Pnma$ phase, and 388 meV/f.u. below that of the cubic $Pm-3m$ structure. Concerning the structural properties of the tetragonal $P4mm$ phase, we determine the following lattice parameters and volume at equilibrium: $a = b = 3.88 \text{ \AA}$, $c = 4.32 \text{ \AA}$, and $V = 65.0 \text{ \AA}^3$, which are in reasonable agreement with our experimental data reported in table 1 of the supplementary information (see composition case $x = 10.0\%$ therein; the existing discrepancies could be due in part to the slightly higher concentration considered in our simulations).

3.2. Raman spectroscopic studies:

Ferroelectric NBT stabilizes at rhombohedral phase ($R3c$), therefore the irreducible representations of the phonons $\Gamma_{\text{opt}} = 4A_1 + 5A_2 + 9E$. A_1 and E modes are both Raman and IR active. Thus, there are 13 Raman active modes

($4A_1$ and $9E$), and five optically inactive or silent modes ($5A_2$) are expected. A Raman spectrum of pure NBT compound in the frequency range $60\text{--}1000\text{ cm}^{-1}$ is shown in supplementary material figure S2. Raman spectra of BT-modified NBT will be discussed later. The Raman spectrum of pure NBT is similar to the reported spectra [8, 35, 36], and three prominent Raman bands are discernible. Using peak-fit, the spectrum is analyzed, and seven modes could be obtained, which are located at 135, 275, 489, 531, 587, 765 and 840 cm^{-1} . Observation of fewer Raman modes than group theoretically predicted could be due to the insufficient intensity of several Raman modes. The low-frequency Raman mode at 135 cm^{-1} corresponds to A–O vibration. The broad and intense band at 275 cm^{-1} is associated with the TiO_6 octahedra whereas the high-frequency modes lying between $650\text{--}950\text{ cm}^{-1}$ are associated with vibrations involving oxygen displacement in TiO_6 octahedral [8, 35]. The high-frequency internal modes at 765 and 840 cm^{-1} are less intense. Raman spectra of unpoled and poled NBT–BT compounds are shown in figures 3(a) and (b), respectively. Spectral features are found to be similar as in pure NBT up to $x = 0.05$, and seven distinct modes could be found in the same frequency range. However, beyond $x = 0.05$, for $x = 0.06\text{--}0.07$, an asymmetric feature develops in higher frequency side for the Ti–O mode at 275 cm^{-1} , and the spectra can be reproduced only by using eight Raman modes (figure 3(a)). As a result, the appearance of a new mode at 317 cm^{-1} (shown by the arrow in figure 3(a)) could be related to a possible structural transition. Upon further increasing composition $x = 0.08\text{--}0.10$, the high-frequency bands located in $400\text{--}700\text{ cm}^{-1}$ become sharper and distinct, and these spectral features can be analyzed by only seven modes, as shown in figure 3(a). For the deconvolution of the Raman spectra, we adopted the strategy of using a minimum number of Lorentzian peaks with a suitable background to reproduce the Raman spectra. Often using more peaks than required leads to a strong correlation of spectral parameters, and their physical interpretation is not meaningful [37].

Raman spectra are sensitive to phase transitions, and often analysis of mode frequency, linewidth, and their integrated intensity are used to identify the structural transition(s) [8, 38, 39]. Figure 4(a) shows the compositional evolution of mode frequencies and line-widths of structurally sensitive low-frequency A–O and B–O modes. One can see that the lattice mode at 135 cm^{-1} shows softening with composition up to $x = 0.08$ and hardening thereafter. The Ti–O vibrational mode shows initial hardening up to $x = 0.05$ and softens thereafter up to $x = 0.10$. Interestingly the line-width of 135 cm^{-1} mode is found to be initially almost same up to $x = 0.04$ and begins to increase at $x = 0.05$, following a decreasing trend at $x = 0.08$. However, the mode at 275 cm^{-1} shows a gradual increase in linewidth up to $x = 0.05$ and then follows a decreasing trend. The discontinuous change in mode frequencies and line widths are typical features for ABO_3 perovskite ferroelectrics undergoing a structural phase transition [8, 38, 39]. Therefore, the present observation of discontinuity in frequencies and linewidth suggest that the NBT–BT perovskite ferroelectric shows a structural transition at $x = 0.05$ and 0.08 compositions, and corroborates the structural transitions as observed

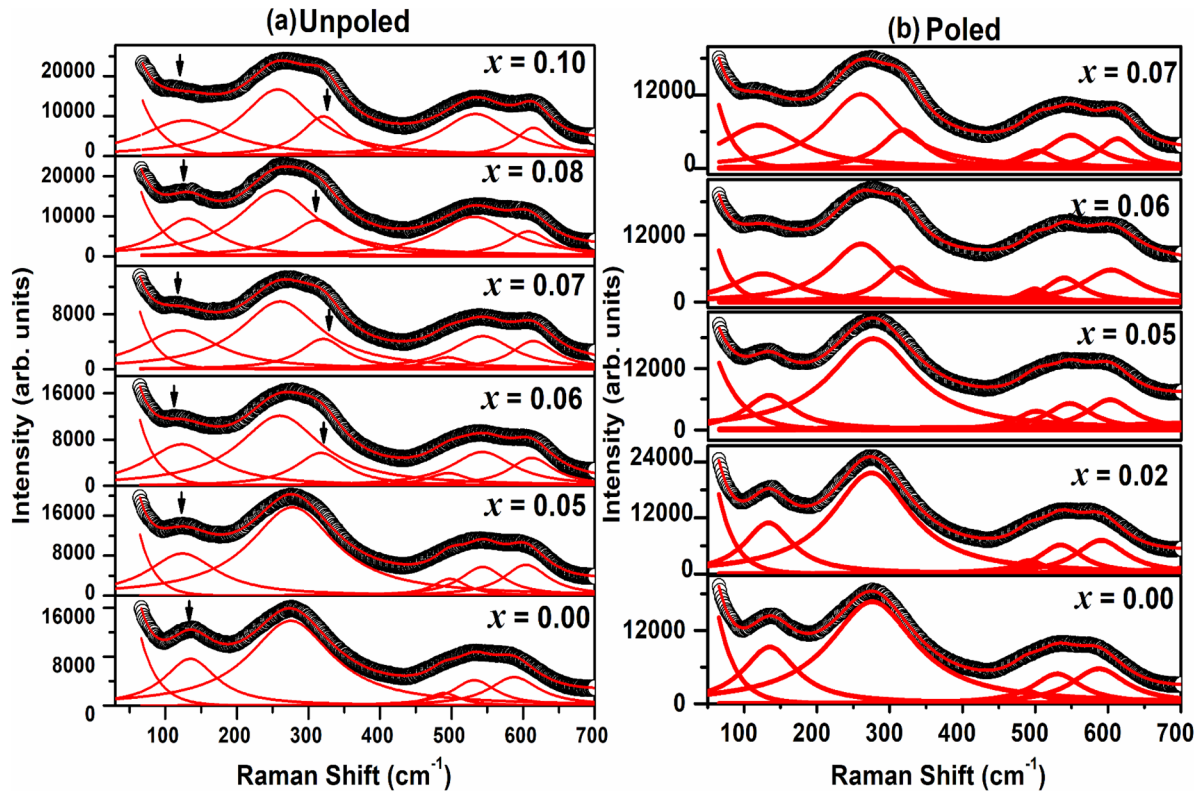


Figure 3. (a) Raman spectra at few selected compositions for unpoled NBT–BT. Multi-Lorentzian peak fitting of Raman spectra are also shown. Open circles represent the experimentally measured data, whereas the solid line represents the fit. (b) Raman spectra at few selected compositions for poled NBT–BT. Multi-Lorentzian peak fitting of Raman spectra are also shown. Open circles represent the experimentally measured data, whereas the solid line represents the fit.

from our XRD studies (discussed earlier). To understand the poling effect on the vibrational behavior of NBT–BT, we have also recorded the Raman spectra of poled NBT–BT compounds (figure 3(b)). The individual deconvoluted and total simulated spectra for a few selected compositions are shown in figure 3(b). The spectra are observed to be similar to the unpoled case except that a comparatively lesser broadening of low-frequency modes at 135 and 275 cm^{-1} is noticed. The effect of a decrease in the broadening of these Raman modes upon poling is discussed below. The lattice mode at 135 cm^{-1} is not identified beyond $x = 0.08$ due to its poor intensity. Like unpoled compounds, for A–O and B–O modes, the evolution of mode frequencies and linewidths with composition show anomalies at $x = 0.05$ and 0.08 composition (figure 4(b)) and point towards the structural transitions.

A close inspection of Raman spectra for both the unpoled and poled samples suggests the possible effect of E-poling on local structural ordering. The Ti–O vibrational band at 275 cm^{-1} becomes symmetric as compared to the corresponding band in the unpoled compound for the same composition, due to the reduction in the TiO_6 octahedral disorder. This behavior is also observed in other reported NBT-based systems [16, 40]. For instance, for $x = 0.02$ poled compound, the linewidth of Ti–O mode (B–O) decreases by nine percent, and that of A–O lattice mode decreases by ten percent as compared to its unpoled case for these same modes. In fact, recent neutron pair distribution function analysis on perovskite system suggests an influence of the degree of disorder of BO_6

octahedra on A–O bonds [16]. Therefore, the observed reduction in the linewidth of A–O and B–O bands as compared to the corresponding unpoled ones is understandable (figures 4(a) and (b)). In other words, E-poling reduces the TiO_6 octahedral disorder, and as a result, it affects the local off-centre displacement of A (Na/Ba/Bi) and B (Ti)-site cations in NBT–BT. This gives rise to more stability of TiO_6 octahedra and our present observation of better ferroelectric loops of the poled NBT–BT system as discussed in detail below.

3.3. Ferroelectric properties

To study the typical ferroelectric behaviours of NBT–BT ceramics ($0.00 \leq x \leq 0.10$), polarization–electric field (P – E) hysteresis loop measurements were carried out at room temperature. The P – E hysteresis loops were measured before and after poling the samples. The ceramic samples were dipped in silicon-oil for poling under application of a suitable dc electric field for few hours. The poling was carried out near the coercive field of each sample. In the present studies, an electric field less than 80 kV cm^{-1} was applied to the specimen to prevent the breakdown of the samples. The characteristic properties such as coercive field $E_C^0 = (E_C^{+0} - E_C^{-0})/2$ and switchable polarization $2P_r^0 = (P_r^{+0} - P_r^{-0})$ were extracted from the P – E loops for all the poled samples. It has been observed that there is a pronounced effect of poling on NBT and NBT–BT composition on the ferroelectric properties of the samples.

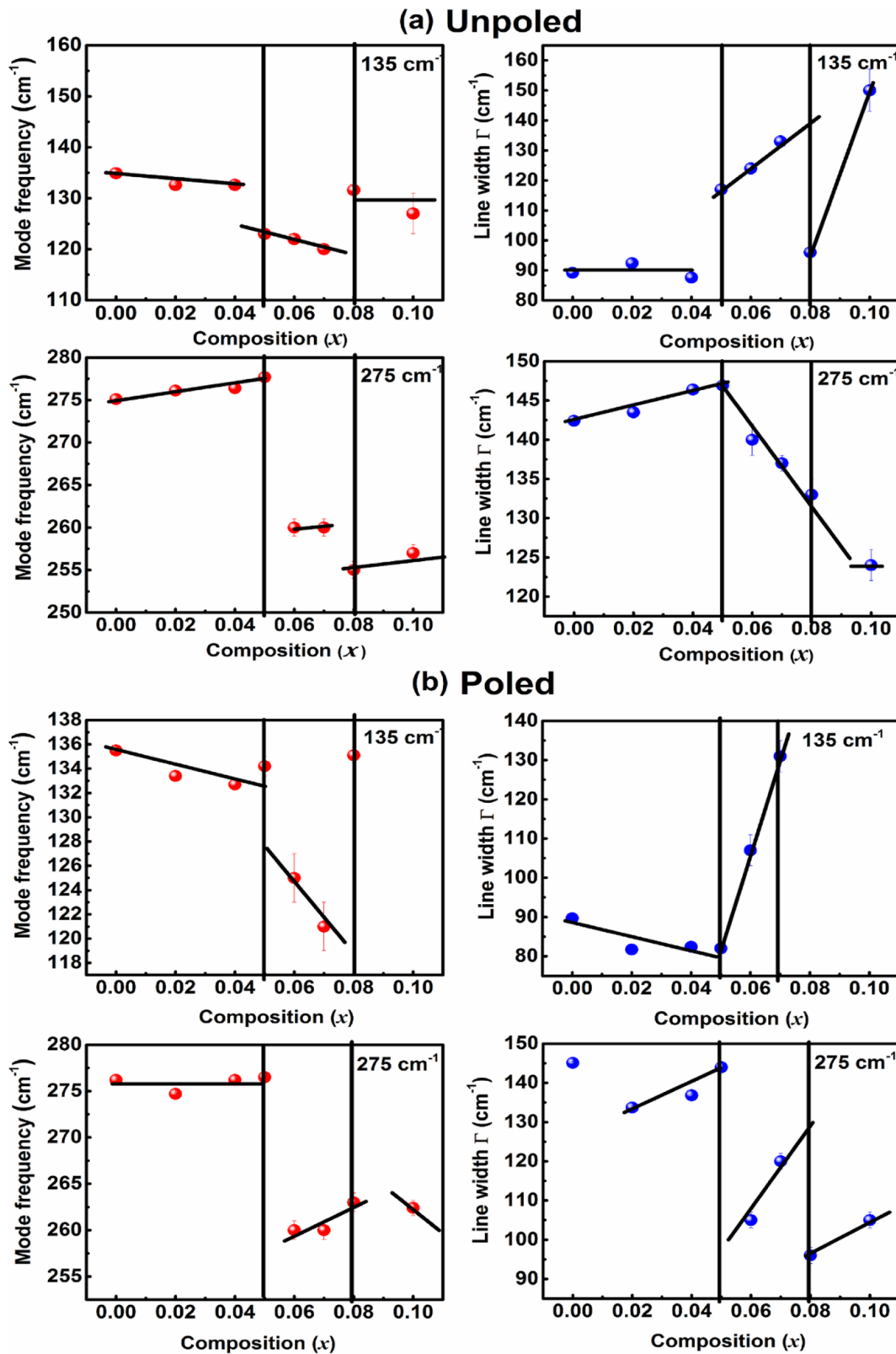


Figure 4. (a) Compositional dependence of Raman mode frequencies and line width of structural sensitive modes (NBT–BT unpoled). Vertical lines correspond to structural transition. (b) Compositional dependence of Raman mode frequencies and line width of structural sensitive modes (NBT–BT poled). Vertical lines correspond to structural transition.

Figure 5(a) showed the P – E hysteresis loop of unpoled and poled NBT–BT ceramics for $x = 0.00$. While figures 5(b)–(d) shows the P – E hysteresis loop of the poled NBT–BT ceramics ($0.02 \leq x \leq 0.10$). The loop as shown in figure 5(a) is observed

to be well developed and possesses a well-defined rectangular shape. The typical rectangular shape of P – E loop as observed in pure NBT (unpoled) is the result of domain switching in the applied electric field and is associated with the long-range

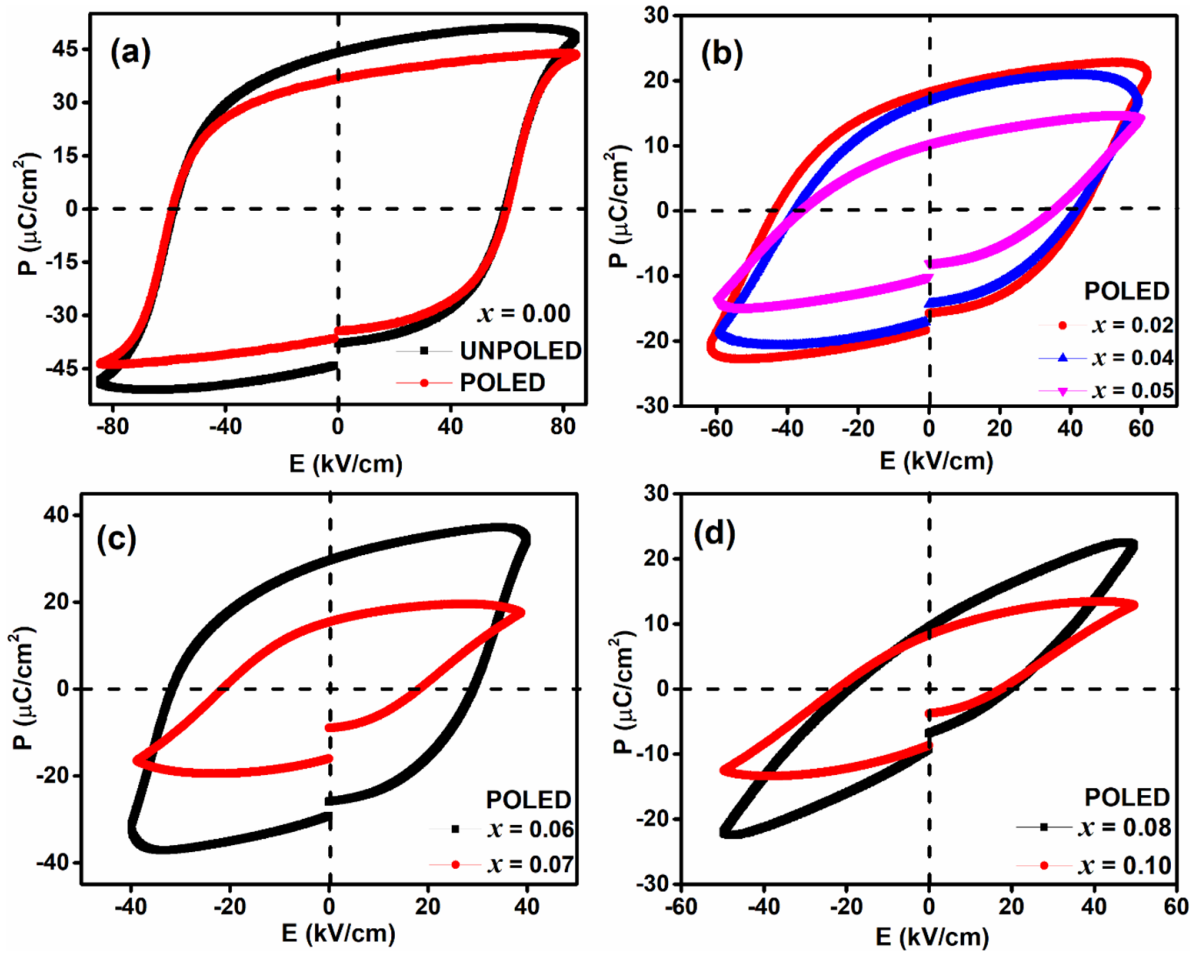


Figure 5. Ferroelectric P - E loop of the solid solution $(1-x)$ NBT $-x$ BT (a) for unpoled and poled sample with $x = 0.00$, (b)–(d) for poled samples with $x = 0.02 \leq x \leq 0.10$.

interaction between dipoles in the ferroelectric micro-domain state [41]. After poling the samples, improvement, and evolution of ferroelectric loops to well-defined real ferroelectric loops is noticed. Similar ferroelectric behaviours have been reported elsewhere [15]. However, in the case of pure NBT, the effect of poling on the nature of P - E loop is small regarding the change in the value of switchable polarization and coercive field. The value of E_C^0 and $2P_r^0$ of the poled NBT samples are estimated as 58.6 kV cm^{-1} and $71.8 \text{ } \mu\text{C cm}^{-2}$, respectively. These values are found to be slightly smaller than the value of NBT single crystal [42]. These results suggest that the present sample is of good quality with nearly ideal stoichiometry. Now the question arises: what is the role of E-poling to obtain a well-defined real ferroelectric loop? On the application of electric field, (i) the randomly oriented domain try to align in the direction of electric field gives rise to a net polarization, (ii) the free charge carriers get sufficient energy to move from one place to another and compensate the deficiencies. This makes the octahedra more perfect and enhances the net dipole moment in the direction of the applied field. Thus, the reduction of domain walls pinning and compensation of defect density on poling gives rise to well saturated ferroelectric loops. Both phenomena contribute to more stable octahedra with minimum local homogeneity leading to the well-defined real ferroelectric loop [15].

Until now we have discussed the effect of E-poling on the P - E loop of unpoled and poled NBT samples. Now we will discuss the effect of E-poling on the BT modified NBT samples. As can be seen from figures 5(b)–(d) for all composition (x), each P - E loop shows well-defined real ferroelectric hysteresis loops upon E-poling. The observation has been well correlated with Raman analysis results. Figure 6 shows the variation of characteristic physical quantities $2P_r^0$ and E_C^0 value as a function of x for the poled sample. For better representation, we have plotted the whole compositional range of poled samples into three parts, (i) Region I for $x = 0.00$ – 0.05 , (ii) Region II for $x = 0.06$ – 0.07 and (iii) Region III for $x = 0.08$ – 0.10 . It is observed that in the Region I, with an increase in x , the values of $2P_r^0$ and E_C^0 gradually decreases. For example, the $2P_r^0$ value decreases from $71.8 \text{ } \mu\text{C cm}^{-2}$ for pristine NBT to $16.8 \text{ } \mu\text{C cm}^{-2}$ for $0.95\text{Na}_{0.5}\text{Bi}_{0.5}\text{TiO}_3$ – 0.05BaTiO_3 (NBT–5BT); and E_C^0 value decreases from 58.6 kV cm^{-1} (NBT) to 35.4 kV cm^{-1} (NBT–5BT) for poled samples. Literature suggests that a lower value of E_C^0 favours easy poling of the ceramics and facilitates polarity switching even at low electric field [7]. The observed decrease in ferroelectric properties up to $x = 0.05$ could be due to a decrease in the rhombohedral distortion, as found in XRD analysis (discussed earlier). Based on the Landau theory, Iwata *et al* [43] reported that the coercive field of the P - E hysteresis

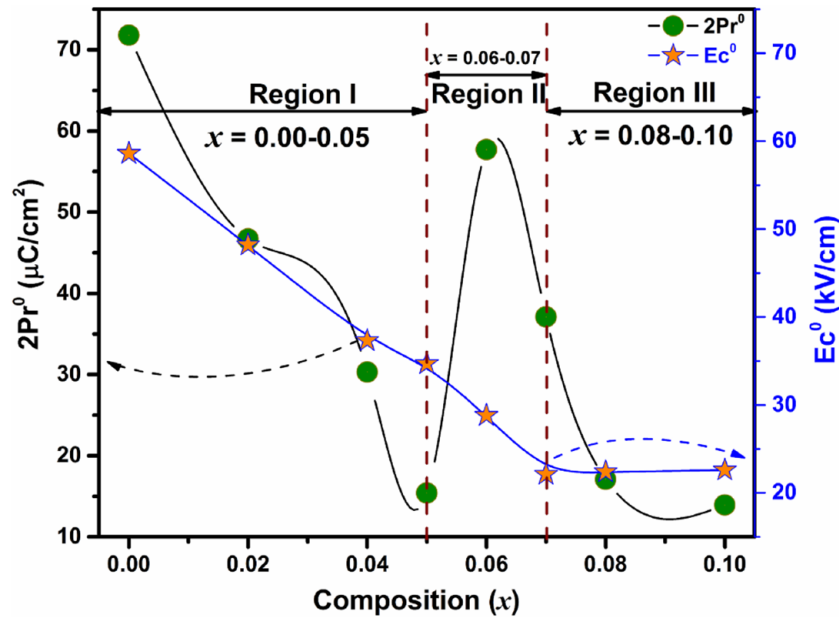


Figure 6. Variation of $2P_r^0$ and E_c^0 with $x = 0.00 \leq x \leq 0.10$ for $(1-x)$ NBT $-x$ BT (for poled sample).

loop becomes extremely small in the vicinity of MPB. This decrease of coercive field with increase in the composition may also be due to the isotropic nature of the free energy function of the polarization component (i.e. decrease of the anisotropic energy of polarization) in the vicinity of MPB. In Region II, an abnormal enhancement in the value of remnant polarization was observed. This enhancement could be due to the existence of the MPB, i.e. the presence of both the rhombohedral and tetragonal dual phases. The dual phase in this compositional range is confirmed from our Rietveld refinement process as discussed in the earlier section. The enhanced switchable polarization near the coexistence region can occur for two reasons: first, as is well known near the morphotropic region in pure PZT, there is often an enhancement for strain and ferroelasticity near the coexistence boundaries, which enhances polarization; and second, although our samples are bulk ceramics, they may indeed exhibit some slight grain orientation. If they are not truly random in orientation, they might present an enhancement due to excess tetragonality near the coexistence boundary. This could be probed further via TEM but is beyond the present study. In the Region III, a decrease in those characteristic values is observed. Pure NBT sample shows the highest value of polarization due to the presence of Bi^{3+} ion. This is expected due to the lone pair effect of 6s valence shell electron in Bi^{3+} ion [37]. In the BT modified NBT, a decrease in the ferroelectric properties can be attributed to the substitution of the large ionic radius of Ba^{2+} ion at A-site of NBT resulting an increase in the lattice parameters and hence disturb the long-range ordering of the Na^{1+} and Bi^{3+} ion. Furthermore, as expected the concentration of ferroelectric active cation Bi^{3+} at A-site of the perovskite decreases with x , and hence one can expect a smaller value of polarization with an increase in x .

3.4. Dielectric properties

Figure 7 shows the variation of relative dielectric constant (ϵ_r) and tangent loss ($\tan \delta$) with temperature at few selected frequencies for $x = 0.0, 0.06, 0.07$ and 0.08 as representatives. Similar observations have also been observed for all other compositions. The dielectric constant decreases with increase in frequency irrespective of the compositions and temperature. This is the signature of polar dielectric materials. The temperature dependent dielectric properties show two distinct anomalies for all compositions, and these anomalies are strongly dependent on the composition. For pure NBT, the 1st dielectric anomaly corresponds to the relaxor-to-ferroelectric (T_{FR}) phase transition observed around 160°C ; whereas the other one, T_{max} observed around 335°C corresponds to the ferroelectric-to-paraelectric phase transition. Around the first dielectric anomaly (T_{FR}), the temperature dependent dielectric properties show the dispersion of the maximum value of dielectric anomaly with frequency (i.e. the maximum dielectric constant shifted towards the higher temperature side with increasing frequency). Similar to the temperature dependent dielectric properties, the dielectric loss also shows an anomaly around the same temperature range of T_{FR} . But the dielectric constant and loss tangent shows reverse behavior with increasing frequency, i.e. at T_{FR} , dielectric constant decreases with increase in frequency whereas dielectric loss increases with increase in frequency, which are observed for all compositions. This type of typical variation of ϵ_r and $\tan \delta$ with frequency at the transition temperature have reported in many classical relaxor ferroelectrics such as PZT, PMN-PT [44, 45]. This transition has also been reported as relaxor ferroelectric phase transitions for $0.94(\text{Na}_{0.5}\text{Bi}_{0.5}\text{TiO}_3)-0.06(\text{BaTiO}_3)$ composition by Jo *et al* [46]. The second anomaly for NBT observed around 335°C

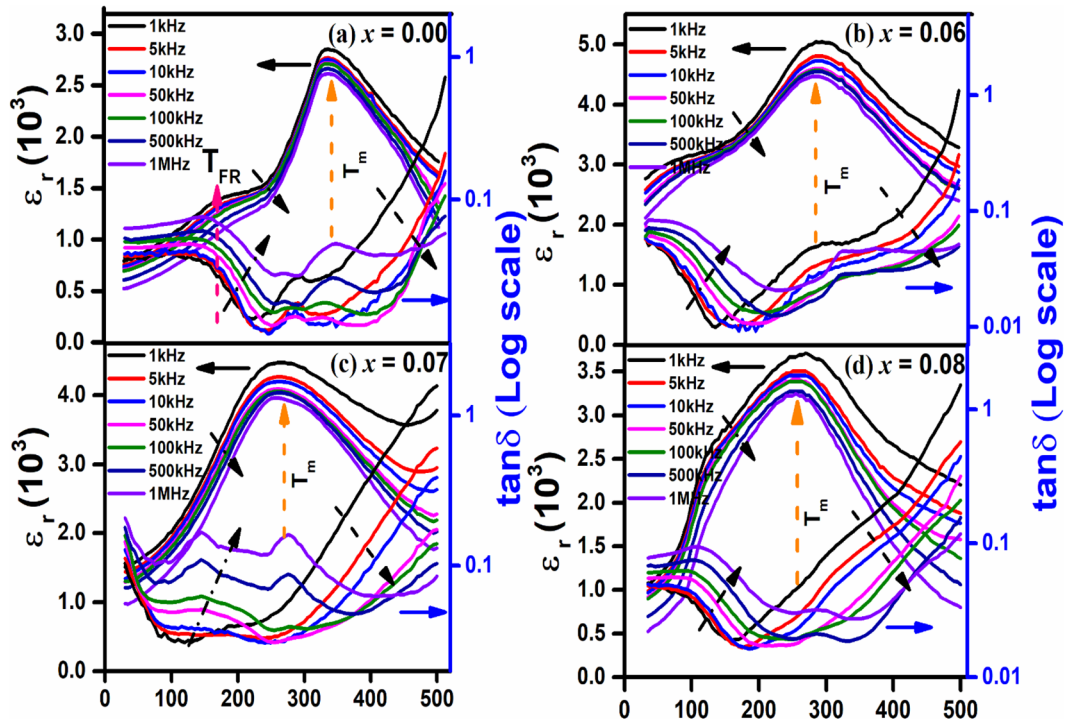


Figure 7. Temperature dependence of relative dielectric permittivity (ϵ_r) and tangent loss ($\tan \delta$) at various frequencies between 1 kHz to 1 MHz for (a) $x = 0.0$, (b) $x = 0.06$, (c) $x = 0.07$ and (d) $x = 0.08$.

corresponds to ferroelectric to paraelectric phase transition temperature (T_m), where maximum dielectric permittivity ($\epsilon_{r,max}$) is independent of frequency, in contrast to the other phase transition. The temperature dependent dielectric loss also shows a peak around the same transition temperature T_m . For this phase transition temperature, both the ϵ_r and $\tan \delta$ decrease with increase in frequency, similar to a classical ferroelectric phase transition. The transition T_m , is reported to be due to the relaxation of polar nano-regions evolved from the rhombohedral phase [46]. The transition temperatures such as T_{FR} , T_m and ϵ_r at T_m are strongly composition dependent, as shown in figure 8. It has been observed that T_m decreases with increase in the compositions, whereas T_{FR} decreases with an increase in the composition up to $x = 0.06$, and after that, it increases. On the other hand, $\epsilon_{r,max}$ increases with an increase in the composition up to $x = 0.06$ but with further increase in the composition it decreases. The maximum value of dielectric constant at T_m and a minimum value of T_{FR} for $x = 0.06$ may be due to the existence of MPB. Around the MPB region, two crystallographic phase $R3c + P4mm$ coexist for $x = 0.06$ and 0.07 . From the DFT calculation, it has been observed that the energy difference between $R3c$ and $P4mm$ crystallographic phase is small. As the energy difference between two crystallographic phases is small, the inter-conversion between two symmetry phases is relatively easy. This will lead to the flattening of the free energy profile, giving rise to the enhancement of polarisation and dielectric constant around the MPB region, as observed from dielectric and ferroelectric properties [46]. The decrease of T_{FR} with composition up to $x = 0.06$ can be explained as follows: with an increase in the composition of BT, there is a transition from crystallographic phase from $R3c$ to $R3c + P4mm$ around the MPB region. The coexistence

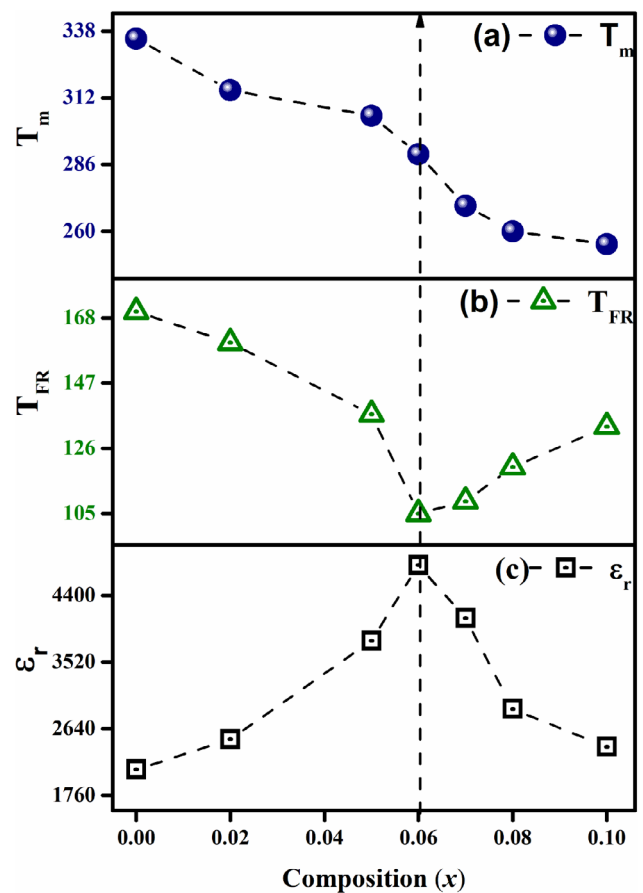


Figure 8. Variation of temperature where dielectric constant is maximum (T_m), relaxor-ferroelectric transition temperature (T_{FR}), relative dielectric permittivity ($\epsilon_{r,max}$) at T_m with composition (x) of $(1 - x)$ NBT - x BT ($0.00 \leq x \leq 0.10$) ceramics.

of two phases at MPB could exert some stress as compared to a single crystallographic phase. This may lead to the decrease of thermal stability of ferroelectric domains, and as a result, T_{FR} may decrease with an increase in composition [47, 48].

4. Conclusions

In summary, solid solutions of $(1-x)\text{Na}_{0.5}\text{Bi}_{0.5}\text{TiO}_3 - x\text{BaTiO}_3$ ($0.00 \leq x \leq 0.10$) ceramics were prepared by sol-gel auto combustion method followed by sintering the ceramics using microwave sintering technique. We report composition driven structural phase transition from $R3c$ to $P4mm$ through the intermediate coexistence of $R3c + P4mm$ near the MPB using Raman spectra and XRD data, which is further corroborated by first-principles calculations. The composition dependent Raman bands position, intensity, and line-width indicate a significant poling effect on local structural ordering as compared to the unpoled one. Near the morphotropic phase boundary composition $x = 0.06$ and 0.07 , an improvement in the ferroelectric properties ($2P_r^0$) was found, as expected due to the complex mixed crystal structure. With an increase in BT composition, there is a decrease in the coercive field from $x = 0.00$ to 0.06 and above that nearly constant until $x = 0.10$. The electric poling effectively improves the concave shape of the hysteresis curves and saturation of polarization loops. Temperature-dependent dielectric properties show two phase transitions which are very much dependent on composition. The highest dielectric constant at T_m was found to be 4800 for $x = 0.06$, which may be due to the proximity of the MPB. We conclude that the incorporation of BaTiO_3 in NBT matrix plays an important role near the morphotropic phase boundary to enhance the ferroelectric and dielectric properties.

Acknowledgments

Authors acknowledge IUAC, New Delhi for the financial and experimental support through project IUAC/XIII.7/UFR-55310 and Dr Banarji Behera School of Physics, Sambalpur University, Jyoti Vihar, Burla for providing experimental facility and fruitful discussion. HSM acknowledges CSIR, India for the SRF fellowship. CC acknowledges support from the Australian Research Council's Future Fellowship funding scheme (project number FT140100135). Computational resources and technical assistance were provided by the Australian Government and the Government of Western Australia through Magnus under the National Computational Merit Allocation Scheme and The Pawsey Supercomputing Centre.

ORCID iDs

Balaram Sahoo  <https://orcid.org/0000-0002-2050-4746>
 J F Scott  <https://orcid.org/0000-0001-6990-8998>
 Dillip K Pradhan  <https://orcid.org/0000-0001-8362-5687>

References

- [1] Haertling G H 1999 *J. Am. Ceram. Soc.* **82** 797
- [2] Jaffe B, Cook W and Jafee H 1971 *Piezoelectric Ceramics* (London: Academic)
- [3] Scott J F 2000 *Ferroelectric Memories* (New York: Springer)
- [4] Rodel J, Jo W, Seifert K T P, Anton E and Granzow T 2009 *J. Am. Ceram. Soc.* **92** 1153
- [5] Panda P K 2009 *J. Mater. Sci.* **44** 5049
- [6] Takenaka T, Marumaya K and Sakata K 1991 *Japan. J. Appl. Phys.* **30** 2236
- [7] Kim J S, Choi B C, Jeong J H, Lee K S and Cho S B 2009 *Ferroelectrics* **384** 120
- [8] Barick B, Mishra K K, Arora A, Choudhary R N P and Pradhan D K 2011 *J. Phys. D: Appl. Phys.* **44** 355402
- [9] Carter J, Aksel E, Iamsasri T, Forrester J S, Chen J and Jones J L 2014 *Appl. Phys. Lett.* **104** 112904
- [10] Ramana M V, Kiran S R, Reddy N R, Kumar K V S, Murthy V R K and Murty B S 2011 *J. Adv. Dielectr.* **1** 71
- [11] Katz J D 1992 *Annu. Rev. Mater. Sci.* **22** 153
- [12] Subbarao E C, Srikanth V, Cao W and Cross L E 1993 *Ferroelectrics* **145** 271
- [13] Ma C, Guo H, Beckman S P and Tan X 2012 *Phys. Rev. Lett.* **109** 107602
- [14] Viehland D, Forst D, Xu Z and Li J 1995 *J. Am. Ceram. Soc.* **78** 2101
- [15] Borkar H, Tomar M, Gupta V, Scott J F and Kumar A 2015 *Appl. Phys. Lett.* **107** 122904
- [16] Maurya D, Pramanick A, Feyngenson M, Neuefeind J C, Bodnar R J and Priya S 2014 *J. Mater. Chem. C* **2** 8423
- [17] Guo H, Ma C, Liu X and Tan X 2013 *Appl. Phys. Lett.* **102** 092902
- [18] He H and Tan X 2005 *Phys. Rev. B* **72** 024102
- [19] Picht G, Töpfer J and Hennig E 2010 *J. Eur. Ceram. Soc.* **30** 3445
- [20] Mohanty H S, Kumar A, Sahoo B, Kulriya P K and Pradhan D K 2018 *J. Mater. Sci. Mater. Electron.* **29** 6966
- [21] Rodríguez-Carvajal J 1993 *Physica B* **192** 55
- [22] Ranjan R and Dwiwedi A 2005 *Solid State Commun.* **135** 394
- [23] Jones G O and Thomas P A 2002 *Acta Crystallogr. B* **58** 168
- [24] Singh S P, Ranjan R, Senyshyn A, Trots D and Boysen H 2009 *J. Phys.: Condens. Matter* **21** 375902
- [25] Garg R, Rao B N, Senyshyn A, Krishna P S R and Ranjan R 2013 *Phys. Rev. B* **88** 014103
- [26] Zuo-Guang Y 2008 *Handbook of Advanced Dielectric, Piezoelectric and Ferroelectric Materials Synthesis, Properties and Applications* (New York: Woodhead Publishing)
- [27] Perdew J P, Burke K and Ernzerhof M 1996 *Phys. Rev. Lett.* **77** 3865
- [28] Kresse G and Furthmüller J 1996 *Phys. Rev. B* **54** 11169
- [29] Kresse G and Joubert D 1999 *Phys. Rev. B* **59** 1758
- [30] Blöchl P E 1994 *Phys. Rev. B* **50** 17953
- [31] Cazorla C and Stengel M 2014 *Phys. Rev. B* **90** 020101
- [32] Cazorla C and Stengel M 2015 *Phys. Rev. B* **92** 214108
- [33] Cazorla C and Íñiguez J 2013 *Phys. Rev. B* **88** 214430
- [34] Cazorla C, Diéguez O and Íñiguez J 2017 *Sci. Adv.* **3** e1700288
- [35] Kreisel J, Glazer A M, Bouvier P and Lucazeau G 2001 *Phys. Rev. B* **63** 174106
- [36] Zhang M S, Scott J F and Zvirgzds J A 1986 *Ferroelectr. Lett. Sect.* **6** 147
- [37] Mishra K K, Satya A T, Bharathi A, Sivasubramanian V, Murthy V R K and Arora A K 2011 *J. Appl. Phys.* **110** 123529

- [38] Mishra K K, Sivasubramanian V and Arora A K 2011 *J. Raman Spectrosc.* **42** 517
- [39] Mishra K K, Arora A K, Tripathy S N and Pradhan D K 2012 *J. Appl. Phys.* **112** 073521
- [40] Rao B N, Datta R, Chandrashekar S S, Mishra D K, Sathe V, Senyshyn A and Ranjan R 2013 *Phys. Rev. B* **88** 224103
- [41] Vittayakorn N and Wirunchit S 2007 *Smart Mater. Struct.* **16** 851
- [42] Suzuki M, Kitanaka Y, Noguchi Y, Akedo J and Miyayama M 2011 *Key Eng. Mater.* **485** 7
- [43] Iwata M and Ishibashi Y 1999 *Japan. J. Appl. Phys.* **38** 5670
- [44] Tagantsev A K 1994 *Phys. Rev. Lett.* **72** 1100
- [45] Wang H, Xu H, Luo H, Yin Z, Bokov A A and Ye Z G 2005 *Appl. Phys. Lett.* **87** 012904
- [46] Jo W, Schaab S, Sapper E, Schmitt L A, Kleebe H J, Bell A J and Rödel J 2011 *J. Appl. Phys.* **110** 074106
- [47] Chen M, Xu Q, Kim B H, Ahn B K, Ko J H, Kang W J and Nam O J 2008 *J. Eur. Ceram. Soc.* **28** 843
- [48] Dai X, Digiovanni A and Viehland D 1993 *J. Appl. Phys.* **74** 3399